UC Santa Barbara
UC Santa Barbara Previously Published Works

Title

Conformational switching of chiral colloidal rafts regulates raft–raft attractions and repulsions

Authors

Miller, Joia M
Joshi, Chaitanya
Sharma, Prerna
et al.

Conformational switching of chiral colloidal rafts regulates raft–raft attractions and repulsions

Joia M. Miller[a], Chaitanya Joshi[a], Prerna Sharma[a,b], Arvind Baskaran[a], Aparna Baskaran[a], Gregory M. Grason[c], Michael F. Hagan[a], and Zvonimir Dogic[a,d,1]

[a]Department of Physics, Brandeis University, Waltham, MA 02454; [b]Department of Physics, Indian Institute of Science, Bangalore 560012, India; [c]Department of Polymer Science and Engineering, University of Massachusetts, Amherst, MA 01003; and [d]Department of Physics, University of California, Santa Barbara, CA 93106

Membrane-mediated particle interactions depend both on the properties of the particles themselves and the membrane environment in which they are suspended. Experiments have shown that chiral rod-like inclusions dissolved in a colloidal membrane of opposite handedness assemble into colloidal rafts, which are finite-sized reconfigurable droplets consisting of a large but precisely defined number of rods. We systematically tune the chirality of the background membrane and find that, in the achiral limit, colloidal rafts acquire complex structural properties and interactions. In particular, rafts can switch between 2 chiral states of opposite handedness, which alters the nature of the membrane-mediated raft–raft interactions. Rafts with the same chirality have long-ranged repulsions, while those with opposite chirality acquire attractions with a well-defined minimum. Both attractive and repulsive interactions are qualitatively explained by a continuum model that accounts for the coupling between the membrane thickness and the local tilt of the constituent rods. These switchable interactions enable assembly of colloidal rafts into intricate higher-order architectures, including stable tetrameric clusters and "ionic crystallites" of counter-twisting domains organized on a binary square lattice. Furthermore, the properties of individual rafts, such as their sizes, are controlled by their complexation with other rafts. The emergence of these complex behaviors can be rationalized purely in terms of generic couplings between compositional and orientational order of fluids of rod-like elements. Thus, the uncovered principles might have relevance for conventional lipid bilayers, in which the assembly of higher-order structures is also mediated by complex membrane-mediated interactions.

self-assembly | membranes | liquid crystals | colloids

When suspended in a bulk isotropic liquid, colloids interact by forces that have steric, electrostatic, or entropic origins (1). In comparison, the same particles suspended in an anisotropic liquid crystals, or at a fluid interface, distort their environment and thus acquire fundamentally different interactions. For example, colloids in a liquid crystal alter the nematic director field, generating topological defects, which lead to unique long-range interactions that drive the assembly of complex architectures (2–5). Colloids bound to oil–water interfaces provide another example in which long-ranged attractive or repulsive interactions are caused by the interface deformations. These in turn are determined by how the interface wets the colloids (6, 7). Lipid membranes provide a complex environment that combines both liquid crystalline-like anisotropy due to the alignment of the fatty chains and interface deformations due to effective 2D confinement (8). Inclusions distort both the membrane thickness and the chain alignment, leading to interactions that are even more multifaceted than those observed for colloids in liquid crystals or on interfaces (9–12). For example, even inclusions with purely repulsive interactions may form stable clusters due to the interplay of overlapping regions of membrane deformation in lipid bilayers (13–16). However, the nanometer size of lipid membranes limits visualizing the nature of membrane-mediated interactions and associated assembly pathways (17–26).

Tunable depletion interactions enable the robust assembly of monodisperse rod-like molecules into colloidal monolayer membranes, structures that mimic many of the properties of the lipid bilayers yet are about 2 orders of magnitude larger (27–30). The 1-μm-thick colloidal membrane allows for direct visualization of inclusions within the membrane and the associated environmental deformations. For example, recent experiments have shown that chiral inclusions dissolved in a colloidal membrane of opposite chirality assemble into colloidal rafts, which are micrometer-sized deformable liquid droplets consisting of a large but precisely defined number of rods (31–33). Here, we show that colloidal rafts can assemble even in achiral membranes and that such rafts can switch between 2 distinct chiral states. Furthermore, we show that interconverting between these 2 conformational states switches the effective raft–raft pair interaction from a long-ranged repulsion to a short-ranged attraction. These conformationally switchable self-assembled mesoscopic structures and interactions drive formation of diverse higher-order reconfigurable assemblages. Using theoretical modeling, we show that the complex interaction behavior can be explained by considering the coupling between the shape of raft interfaces and the tilt field of colloidal rods within the membrane. We find that a minimal symmetry-based model of phase-separated and tilted membranes qualitatively describe most

Significance

We describe hierarchical assemblages of colloidal rods that mimic some of the complexity and reconfigurability of biological structures. We show that chiral rod-like inclusions dissolved in an achiral colloidal membrane assemble into rafts, which are adaptable finite-sized liquid droplets that exhibit 2 distinct chiral states of opposite handedness. Interconverting between these 2 states switches the membrane-mediated raft interactions between long-ranged repulsions and attractions. Rafts with switchable interactions assemble into analogs of electrostatic complexation observed in charged particulate matter. Our results demonstrate a robust pathway for self-assembly of reconfigurable colloidal superstructures that does not depend on tuning the shape and interactions of the elemental units, but rather on the complexity of the emergent membrane-mediated interactions.

of the experimental observations. Our results demonstrate how properties of the membrane environment can be tuned to generate complex self-assemblages from structurally simple building blocks.
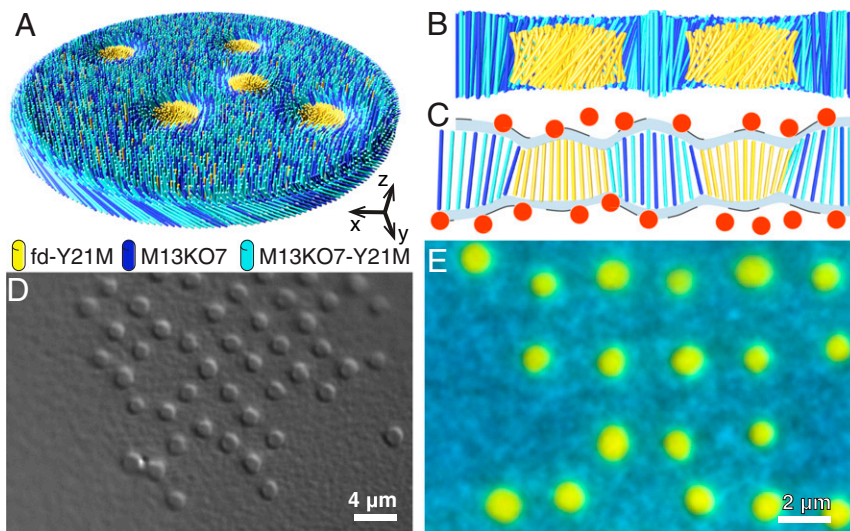
Assembly of Rafts in Achiral Colloidal Membranes

We used M13KO7 and *fd* bacteriophage, which are both rod-like colloidal particles with ~7-nm diameter and 2.8-μm persistence length (34). M13KO7 is 1,200 nm long, while *fd-wt* is 880 nm long. Addition of a nonadsorbing polymer to a virus solution induces attractive interactions, causing the viruses to assemble into colloidal membranes, which are liquid-like monolayers of rods, aligned lengthwise, with lateral dimensions reaching hundreds of microns (27, 28). Local twisting of rods as preferred by their intrinsic chirality is fundamentally incompatible with the global constraints of the 2D membrane geometry. Consequently, all of the rods within the membrane interior are forced into a higher-energy untwisted state, while rods within a twist penetration length of the membrane edge are free to twist and thus lower their energy (35). This frustration leads to chiral control of the membrane edge tension (36).

As evidenced from studies of bulk cholesteric liquid crystals, aligned viruses lower their interaction energy by slightly twisting with respect to each other (37, 38). A single amino acid mutation of the major coat protein turns the wild-type left-handed M13KO7 or *fd-wt* virus into a distinct filament class, denoted by M13KO7-Y21M and *fd*-Y21M, which are both stiffer than the wild-type rods and right-handed (39). Varying the ratio of Y21M-*wt* viruses controls the magnitude of the cholesteric pitch in bulk liquid crystals and the effective chirality of the colloidal membranes. In a weakly chiral limit, the rods at the membrane's edge form alternating domains of left- and right-handed twist that are separated by point-like defects (40). The rod chirality controls the effective line tension of the domains of either handedness, which in most cases induces difference in the size of left- and right-handed domains (36). However, for achiral membranes, the do-

mains of either handedness have the same spacing. This criterion reveals that colloidal membranes composed of 63% Y21M and 37% *wt* rods are effectively achiral. Based on these findings, we define the chiral parameter: $\phi_{ch} = (r_{M13KO7} - 0.37)/0.63$, where $r_{M13KO7} = n_{M13KO7}/(n_{M13KO7} + n_{M13KO7-Y21M})$, is the fraction of left-handed rods, and n_{M13KO7} and $n_{M13KO7-Y21M}$ are the concentrations of long rods. For achiral mixtures, $\phi_{ch} = 0$, while $\phi_{ch} = 1$ indicates maximally left-handed rod composition. Achiral colloidal membranes composed of fd-*wt* and fd-Y21M exhibit an edge instability that is consistent with the absence of rod twist (40).

Colloidal membranes comprised of a uniform mixture of rods of opposite chirality, such as M13KO7 and *fd*-Y21M, force the constituents within the membrane interior to untwist. However, rods with opposite chirality and different lengths can form chiral colloidal rafts that allow the twist to penetrate the membrane interior and thus lower the system free energy. These colloidal rafts are finite-sized equilibrium droplets of 1-handedness and length that coexist with the background membrane of the opposite handedness and different thickness (31). The finite twist at a raft's edge decays into the membrane bulk, driving long-range repulsive interactions between the rafts (41).

To study the effect of chirality on the raft stability, we systematically lowered the net chirality of the background membrane by mixing 2 types of rods (M13KO7 and M13KO7-Y21M) of equal length but opposite chirality. We dissolved short weakly chiral right-handed *fd*-Y21M in such achiral long-rod background membranes. Despite the weak chirality, the short rods still robustly assembled into micrometer-sized rafts (Fig. 1). These rafts in isolation were structurally similar to previously studied rafts formed in the chiral limit, $\phi_{ch} = 1$ (31). However, there was 1 major difference. In the chiral limit, rafts experienced long-ranged repulsive interactions. Consequently, they exhibited liquid order at lower densities and colloidal crystals at higher densities. In contrast, rafts in achiral membranes formed clusters, while leaving other spaces void, thus suggesting attractive interactions

Fig. 1. Self-assembly of rafts in an achiral membrane. (*A*) Schematic illustration of a colloidal membrane composed of an achiral mixture of long left-handed rods (M13KO7; dark blue), long right-handed rods (M13KO7-Y21M; light blue), as well as a small fraction of short right-handed rods (*fd*-Y21M; yellow); short rods form micrometer-sized rafts suspended in the membrane background. (*B*) *x*–*z* cross-section of a colloidal membrane containing a raft pair. (*C*) The rods in a colloidal membrane are held together by the osmotic pressure exerted by the enveloping polymer suspension indicated in red. The presence of a colloidal raft leads to variations in the membrane thickness. The depleting polymers are excluded from the membrane interior and from a layer adjacent to the membrane surface (indicated in gray). The latter leads to an effective surface tension that disfavors height variations. (*D*) DIC micrograph of a dense raft cluster coexisting with an empty background membrane suggests the presence of attractive raft–raft interactions. Raft clusters tend to form square lattices. (*E*) Fluorescence image of a cluster of rafts with square-like ordering observed in an achiral membrane. Raft-forming short right-handed rods (*fd*-Y21M) are indicated in yellow. The background membrane is composed of an achiral mixture of long left- and right-handed rods (M13KO7 and M13KO7-Y21M, respectively). Left-handed long rods are labeled and shown in blue.
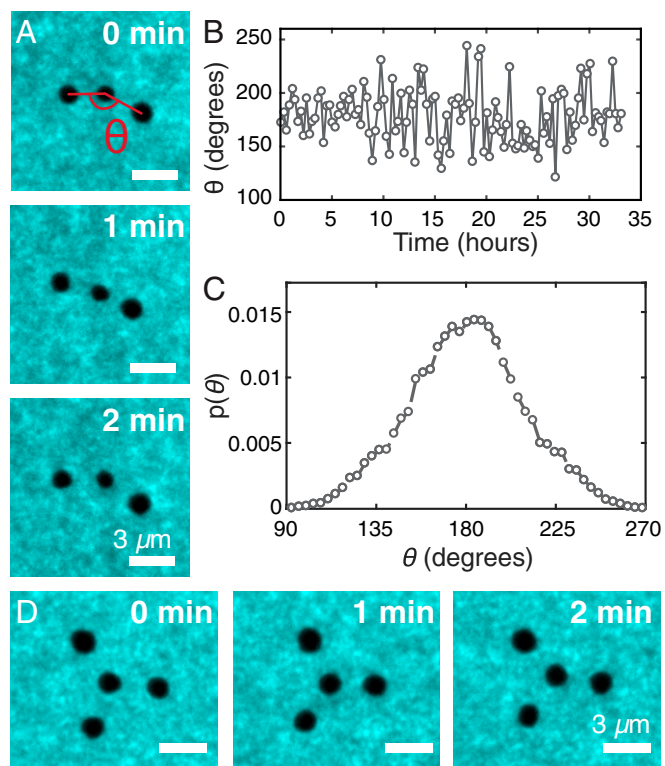
Fig. 2. Rafts form stable trimers and tetramers. (*A*) A 3-raft cluster forms a stable trimer that assumes the shape of an isosceles triangle, with the large angle denoted as θ. (*B*) Plot of angle θ extracted from a fluctuating trimer as a function of time. (*C*) Probability distribution function $p(\theta)$, extracted from a time series of a fluctuating trimer. (*D*) A 4-raft cluster forms a distinct and highly stable tetrameric structure, wherein 3 outer rafts are evenly spaced around a center raft.

(Fig. 1*D* and Movie S1). Furthermore, at higher densities raft clusters formed square crystalline lattices, hinting at the presence of complex interactions (Fig. 1*E*).

We observed intriguing behaviors even at low densities, where only a few rafts interacted with each other. For example, 3 colloidal rafts formed obtuse and isosceles triangle-like structures, which exhibited large shape fluctuations centered around a straight line of rafts (Fig. 2 *A–C*). Such configurations remained stable over the entire sample lifetime and never transformed into an equilateral configuration (Movie S2). This suggests that raft interactions are not simple pairwise-additive attractions, which would yield clusters with the shape of an equilateral triangle. Four-raft clusters assumed another unusual yet highly stable architecture that cannot be explained by simple attractions. Specifically, we observed a central raft that was surrounded by 3 outer rafts, arranged into an equilateral triangle (Fig. 2*D* and Movie S3). These observations further suggest complex raft–raft interactions with an attractive component.

Measuring Raft–Raft Interaction Potentials

Motivated by these observations, we directly measured the pairwise potentials between colloidal rafts. Since short-rod rafts are repelled from a focused light, we used a time-shared optical trap arranged into a plow (31). Bringing 2 rafts into close proximity and shutting of the traps revealed 2 distinct behaviors: Some pairs remained bound for the entire observation time, while other pairs drifted apart from each other over a matter of seconds (Fig. 3 *A* and *B*). To quantify interactions, we used the blinking optical trap (BOT) technique (42). We brought rafts together with the optical plows and quantified their subsequent
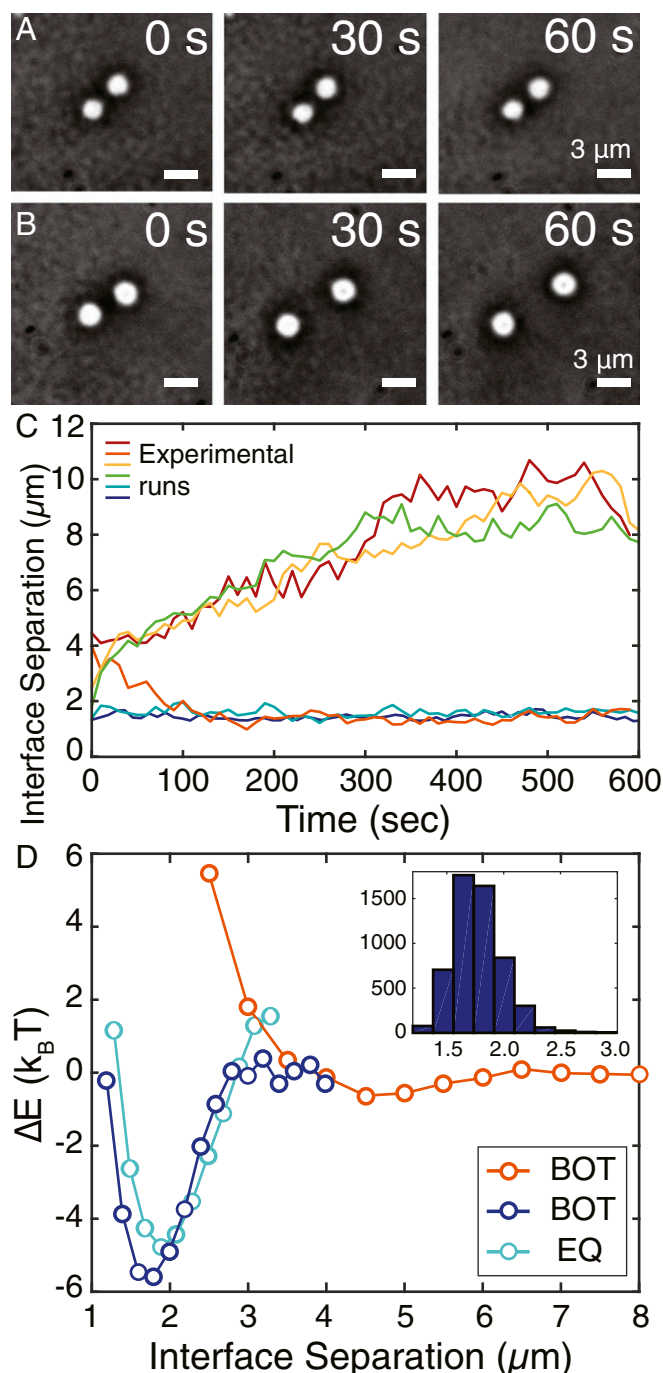

Fig. 3. Raft interactions can switch between attractive and repulsive. (*A*) Upon being brought into close proximity with an optical plow, 2 rafts form a stable pair. (*B*) For identical conditions, a different raft pair repels each other. (*C*) Trajectories of several raft pairs brought into close proximity with optical plows. The data illustrate the existence of 2 categories of raft interactions that are either attractive or repulsive. (*D*) Effective interaction potentials for attractive and repulsive rafts that are extracted from the raft trajectories using the blinking optical trap (BOT) technique. Stable pairs have a potential minimum at 1.6-μm edge separation; unstable pairs have an exponentially repulsive potential, characterized by a ~0.6-μm length scale. (*Inset*) The histogram of raft separations for an attractive raft pair. Attractive interactions extracted from equilibrium fluctuations agree with the BOT measurements to within an arbitrary constant.

trajectories. The laser was shuttered before taking any measurements to avoid the effects of trap-induced membrane distortions (Fig. 3C and Movie S4). Acquiring many trajectories yielded 2 distinct transition probability matrices. One describes an exponentially repulsive interaction with a length scale of ~0.6 μm, which is similar to interactions in the previously studied chiral membranes (31) (Fig. 3D). The other corresponds to a ~6 k_BT attractive well with a well-defined minimum at 1.6-μm raft edge separation. The latter results were confirmed by tracking isolated attractive raft pairs, in equilibrium, over a period of time. These measurements generated the effective probability distribution function of the raft pair separation, $p(r)$. Inverting with the Boltzmann relationship, $\Delta V(r) = -k_BT \log p(r)$, yielded a similar potential, within an unknown constant due to an unidentified zero point (Fig. 3D). When using the BOT technique, a pair that was stably attractive in 1 experimental run could be repulsive in the next. Similarly, a previously repulsive pair could bind after the laser was shuttered. These measurements demonstrate that rafts in an achiral membrane background exist in 2 conformational states with distinct attractive and repulsive interactions. Rafts switched between 2 interaction types only when being manipulated with an optical trap due to deformations of the surrounding membrane. Left on their own rafts remained in 1 state on experimental timescales, which suggests that the kinetic barrier associated with handedness switching cannot be overcome by thermal fluctuations.

Raft Structure Determines Raft Interactions

To reveal the structural origin of switchable raft interactions, we visualized raft-induced distortions of the background achiral membrane using LC-PolScope, a technique that quantitatively images the sample optical retardance (43). For a monolayer membrane lying in the image plane, retardance is proportional to rod tilt away from the membrane normal (Fig. 4A). Regions in which the rods are aligned along the membrane normal appear dark in LC-PolScope images. Rods tilted away from the normal have structural and optical anisotropy and thus appear bright (Fig. 4A). Previously, LC-PolScope microscopy visualized how twist penetrates the membrane interior over a characteristic length scale (35). When viewed with LC-PolScope, rafts in the achiral membrane appeared bright, indicating local twist (Fig. 4 C and E). However, there was no obvious difference in the appearance of the attractive and repulsive raft pairs.

Since it only measures the rod tilt away from the z axis, LC-PolScope with normal incident illumination does not reveal the handedness of chiral rafts. To measure raft handedness, we instead illuminated the sample with the light incident at an angle θ with respect to the membrane normal (Fig. 4B). Rods with positive local tilt in y–z plane were then more aligned with the incident light. They thus had lower apparent retardance and appeared darker in the LC-PolScope image. In comparison, rods with negative tilt in the y–z plane tilted away from the incident light at a larger angle. Having higher apparent retardance, they
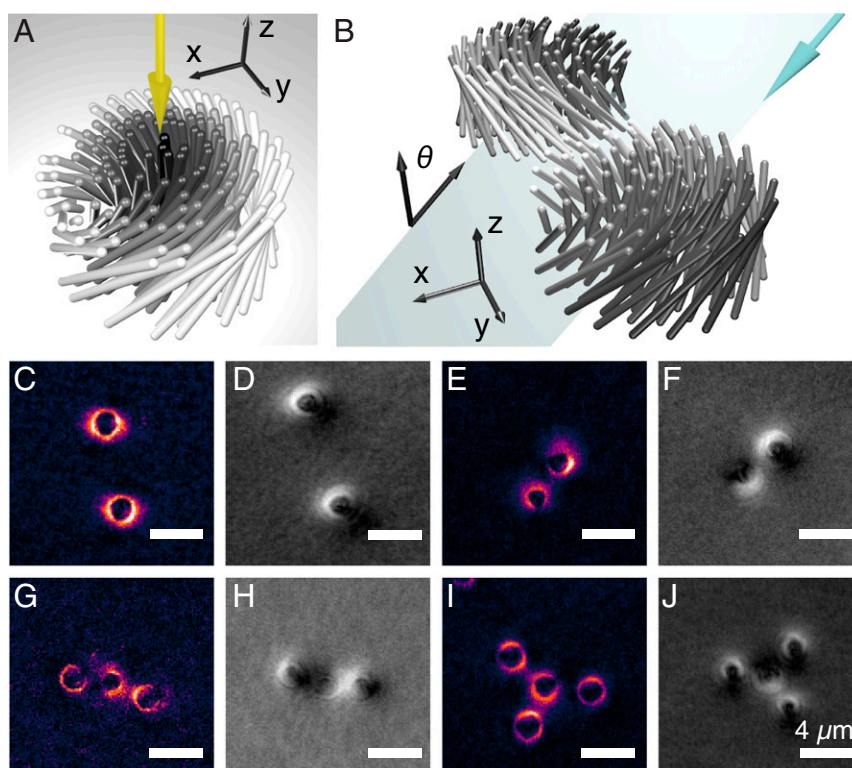
Fig. 4. Raft twist determines their interaction. (A) Schematic of a twisted raft viewed with LC-PolScope. At the raft center, rods are aligned with the incoming light, leading to zero retardance signal. Increasing the tilt away from the raft center leads to brighter signal in LC-PolScope. Normal illumination does not distinguish between the handedness of raft twist. (B) Tilting the incoming light along the x axis with angle θ causes rods tilted along or against the incoming light to have different effective retardance values. When viewed with LC-PolScope, rods tilted with angle −θ are bright while rods tilted with angle θ appear dark. For right-handed rafts, this corresponds to bright signal at the back of the raft and dark at the front. These intensities are opposite for left-handed rafts, thus allowing us to differentiate between handedness of the raft twist. (C and E) Normal incidence LC-PolScope images of an attractive and repulsive raft pair. (D and F) Tilted incidence LC-PolScope shows that both rafts are bright at the top in a pair of repulsive rafts, while rafts are bright at the top and bottom in an attractive pair. Hence, repulsive and attractive pairs have the same and opposite handedness, respectively. (G) Normal incidence LC-PolScope of a stable trimer. (H) Tilted LC-PolScope reveals that the central raft has opposite handedness from the 2 outer rafts. (I) Normal incidence LC-PolScope of a stable tetramer. (J) Tilted LC-PolScope reveals that the central raft has opposite handedness from the 3 outer rafts.

appeared as brighter regions. Therefore, colloidal rafts imaged with a tilted angle LC-PolScope have an apparent asymmetry, which could be used to determine their handedness. Right-handed rafts appeared brighter on top and darker on the bottom, while the appearance of left-handed rafts was the reverse. Using combined tilted and normal incidence LC-PolScope revealed both the maximum raft twist and the twist handedness. All isolated rafts, as well as repulsive raft pairs, had internal right-handed twist, which is favored by the right-handed chirality of *fd*-Y21M (Fig. 4 *C* and *D*). In contrast, each raft in an attractive raft pair had opposite handedness, despite 1 raft being in a higher-energy counter-twisted state (Fig. 4 *E* and *F*). Normal-incidence LC-PolScope demonstrated that the maximum edge twist was of similar magnitude for rafts of either chirality (Fig. 4 *C* and *E*). Trimers and tetramers also included a counter-twisted central raft, which was surrounded by 2 or 3 right-handed rafts, respectively. The outer rafts repelled each other but were bound to the central raft with the opposite chirality (Fig. 4 *G–J* and Movie S5).

The colloidal membrane background is achiral, and the rafts composed of *fd*-Y21M rods are weakly right-handed. Thus, right-handed twist should be thermodynamically favored by the intrinsic chirality of raft rods, while isolated counter-twisted left-handed rafts must be higher-energy metastable structures. Most isolated rafts were right-handed (Fig. 5*A*), and the number of counter-twisted rafts only became comparable to that of rafts with favorable twist at very high raft densities, such as in a square lattice. Using an optical trap, we isolated a counter-twisted raft by separating an attractive L-R pair, and subsequently observed its dynamics. The handedness, retardance, and size of this raft remained unchanged throughout the entire observation period, demonstrating that the barrier to switching into lower-energy twist state must be significant (Fig. 5 *B–D* and Movie S6). Using optical manipulation, we also assembled exotic clusters not found in equilibrium sample, such as a trimer with a lower-energy central raft that was bound to 2 outer counter-twisted rafts (Movie S7).
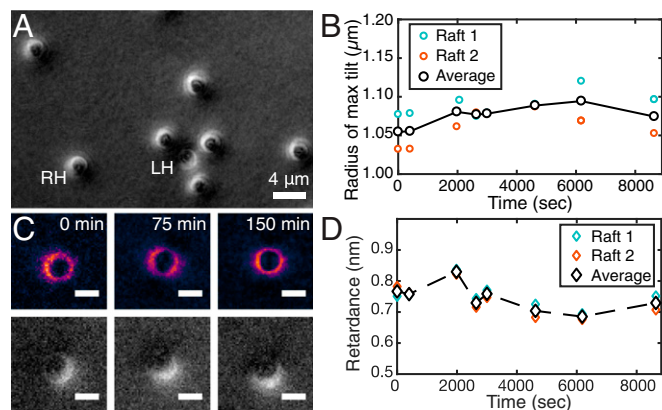
Continuum Model of Raft Interactions

To gain insight into the structural origin of switchable raft interactions, we employed theoretical modeling. Previously developed continuum models for binary membranes explained the assembly and repulsive interactions of chiral rafts in a membrane of opposite chirality (32, 33, 41). However, since the stability and

Fig. 5. Isolated counter-twisted rafts are metastable in achiral membranes. (*A*) Tilted incidence LC-PolScope of isolated rafts and a tetramer illustrates that isolated rafts have favorable right-handed twist. (*B*) Time sequence of an isolated counter-twisted raft shown in both normal and tilted incidence LC-PolScope. (*C*) The size of a counter-twisted raft does not change with time. (*D*) The maximum tilt as measured by retardance of a counter-twisted raft does not change with time.

direction of twist of rafts in these models is assumed a priori to be driven by chirality, they cannot explain the metastability of counter-twisted rafts observed here. Hence, the experimental observations of metastable rafts of both handedness imply that additional mechanisms must be at work to destabilize the rafts to spontaneous twist, even in the absence of intrinsic chirality. Further experiments (described below) indicate that the counter-twisted rafts become less stable upon increasing the left-handed chirality of the background membrane. This suggests that as chirality increases, one handedness is biased over the other, until the counter-twisted raft becomes unstable. The microscopic origin of this physical mechanism can be traced to the length asymmetry of the rods and the shape of a twisted raft-background domain edge. The depletant has more accessible volume for twisted short rod rafts, which drives the edge unstable to twist of either chirality, and gives rise to a barrier for transitions between configurations with opposite twist. A detailed calculation of the relationship between raft geometry and depletion interaction strength will be presented in a future paper. The key goal of the present study is to understand the physical mechanisms underlying the complex interactions between like and opposite twist domains.

To this end, we have extended the previously developed Ginzburg–Landau model to include a minimal model of edge–tilt coupling that can drive a raft unstable to spontaneous twist independent of the intrinsic chirality. The model accounts for the liquid crystalline elastic energy, coupling between variations in the local height of the membrane and the depletion interactions, and coupling between twist of the director field and compositional fluctuations. Membrane configurations are described by 2 fields: a director field $\hat{n}(r)$ that denotes the orientation of the rods relative to the membrane normal (assumed to be $\hat{z}$, with $\cos\theta = n_z$), and a concentration field parameter $\phi(r)$, which characterizes the local difference in the densities of short and long rods. The free energy is given by the following:

$$F\Big/k_{\mathrm{B}}T = \int d^2r \left[\frac{1}{2}K_1(\nabla\cdot\hat{n})^2 + \frac{1}{2}K_2(\hat{n}\cdot\nabla\times\hat{n} - q(\phi))^2 \right.$$
$$+ \frac{1}{2}K_3(\hat{n}\times\nabla\times\hat{n})^2 + \frac{1}{2}C\sin^2\theta - \frac{\phi^2}{2} + \frac{\phi^4}{4}$$
$$\left. + \frac{\epsilon_\phi}{2}(\nabla\phi)^2 - \frac{\gamma}{2}\sin^2\theta(\nabla\phi)^2 + \frac{C_2}{4}\sin^4\theta \right]. \quad [1]$$

The first 3 terms describe the Frank elastic energy associated with distortions of the director field, with K_1, K_2, and K_3 as the splay, twist, and bend elastic moduli. The local twist is coupled linearly to the concentration field ϕ, $q = q_0 + a\phi$, where $q_0 \pm a$ corresponds to the preferred twist of the short rods and long rods, respectively. For the achiral background, q_0 is set to a. The fourth term describes the free energy cost of rod tilt arising from depletion interactions, with C as the bulk depletion modulus, which is proportional to the applied osmotic pressure. This term favors rods in the membrane interior to align with the membrane normal. The next 3 terms in even powers of ϕ account for the tendency of short and long rods to phase separate, with ε_ϕ being the line tension that penalizes the long–short rod interface. Everything up to this point was included in the previously developed model (33). The penultimate term provides a mechanism for the raft edge-twist instability. While this term should be expected due to the most generic coupling between tilt and composition, here we note that such a term can arise due to the exclusion of the depletant from a surface layer around the membrane, which leads to a free energy penalty $F_A = \prod aA$, where $\prod$ is the osmotic pressure of the depletant, and the excluded layer has a volume aA, with a, the depletant radius, and A, the membrane surface area (32, 44). The surface area increases due to variations in the membrane height

according to $A = 2 \int d^2r \sqrt{1 + (\nabla h)^2}$. The membrane height depends on both the local tilt and composition, $h(r) = t_\phi n_z$, with t_ϕ as the composition-averaged half-length of the rod—t_ϕ interpolates linearly between t_s and t_l as ϕ goes from $+1$ to -1. Incorporating the dependence of membrane height on local composition and expanding to second order in ϕ, results in a term $-\gamma \sin^2 \theta (\nabla \phi)^2$, with $\gamma \sim \Pi$. Notably, this term favors spontaneous twist and is independent of chirality. It thus serves a proxy for an edge–tilt coupling that renders rafts unstable to twist. The final term must be added for stability, with C_2 as an adjustable parameter.

We tested the ability of our model to describe the experimental observations. We set $K_2 = K_3 = C = 1$ and varied the splay elastic constant, K_1, and the surface tension, γ. Geometrical arguments suggest that $K_1 > K_2$ and $K_2 = K_3$, but there have been no experimental measurements of the Frank elastic constants for these components (45). Quasistatic calculations estimated the raft stability (*SI Appendix*, Fig. S4). We fixed the radius and composition profile of a raft and calculated the equilibrium director field by minimizing the free energy (Eq. **1**). To determine the dependence of the free energy on raft size, we performed this calculation over a range of raft radius values. We found a range of K_1, γ values over which right-twisted rafts with finite radius are stable, and counter-twisted rafts are metastable. In particular, for the value of splay constant used in this work, $K_1 = 3$, counter-twisted rafts are metastable for $\gamma \geq 0.5$. Above a threshold value of chirality, $a = 0.05$, the metastable counter-twisted state disappears, consistent with previous studies with chiral background membranes that do not exhibit counter-twisted domains.

Next, we performed an analogous procedure to calculate the interactions between raft pairs. We imposed a composition profile corresponding to 2 rafts with fixed radius and separated by distance d, and then optimized the free energy with respect to the director field. Our model predicts repulsive and attractive interactions for like-twisted and opposite-twisted raft pairs, respectively (Fig. 6 *C* and *D*). Comparison of the theoretical results with experiments shows that the model captures most key features: stable twisted rafts independent of chirality, metastability of counter-twisted rafts at low chirality, and attractive/repulsive interactions between pairs of opposite/like twisted rafts. Importantly, we could not find a parameter range in which the model simultaneously captures all of these features without including an edge–tilt coupling, supporting our hypothesis that such an effect is essential for the switchable interactions observed in the experiments. Notably, the qualitative form of the raft–raft interaction depends only on the relative twist direction of the 2 rafts: a pair of rafts with the same twist direction always has repulsive interactions, whereas a pair of rafts with opposite twist direction always has attractive interactions. We identify 1 discrepancy with experiment—the theory does not predict the short-range repulsions of oppositely twisted rafts. This limitation may arise from an additional cost of through-thickness density variation in splayed regions that form between opposite twist domains, which will be investigated in a future work. We also
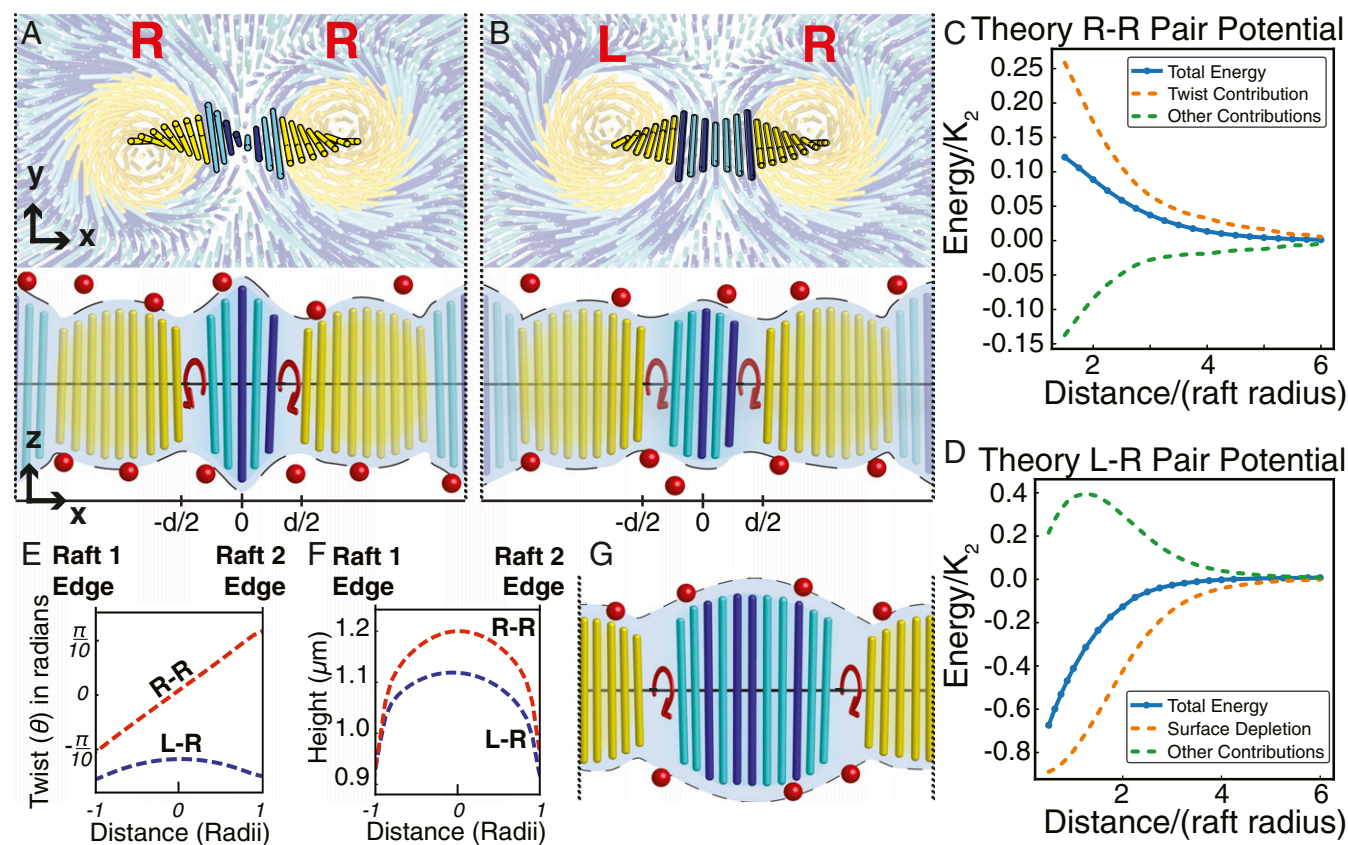
Fig. 6. The theoretical model shows that raft attractions arise from minimizing surface area in left- and right-handed pairs. (*A* and *B*) Schematic representations of rod twist between rafts from above and from the side for pairs of rafts with the same (R-R) and opposite (L-R) twist. (*B*) Edge twist direction. Model results for energy cost vs. distance between rafts in terms of their radii show surface costs dominate in both cases, leading to repulsive interactions for R-R pairs (*C*) and attractive interactions for L-R pairs (*D*). (*E* and *F*) Theoretical twist and height profiles respectively between 2 rafts given a separation distance equal to 2.0 raft radii. (*G*) Schematic representation of twist relaxation for noninteracting rafts. Parameters used in the calculations are as follows: $K_1 = 3.0$, $K_2 = K_3 = C = 1$, and $\gamma = 0.8$.

note that our quasistatic calculation assumes a fixed raft shape, whereas the experiments show that raft shapes deform.

To understand the origin of the switchable interactions, we first consider the repulsive interactions between rafts of the same chirality in an achiral membrane background (Fig. 6C). We consider the twist field within and surrounding 2 right-handed interacting rafts. Due to the coupling of the local membrane thickness to the local rod twist, each raft distorts the membrane–polymer interface in its immediate vicinity. This is reminiscent of interactions between interfacially adsorbed colloids, which generally attract each other since bringing particles closer together reduces the overall area of the distorted interface (6). Based on such reasoning, one might expect that colloidal rafts will also experience attractive interactions, driven by the effective interfacial distortion energy. However, our model predicts, and we also experimentally measure strong repulsive interactions. This can be explained by the intrinsic coupling between the membrane height and the rod twist, which is absent in simple liquid–liquid interfaces. We define the local tilt field, $\theta(x,y)$, with the origin of the coordinate system at the midpoint between 2 rafts separated by distance d. The twist at the edges of a pair of right-handed rafts, designated an R-R pair, is $\theta(-d/2,0) = -\theta_0$ and $\theta(d/2,0) = \theta_0$, where θ_0 is the maximum twist angle at the raft boundary (Fig. 6A). Consequently, the rods in the background membrane between the 2 rafts have to distort from $-\theta_0$ to θ_0 over a distance d, and the twist field crosses zero at the midpoint, $\theta(0,0) = 0$. In essence, rods at the midpoint between rafts must untwist, regardless of the raft separation (red line in Fig. 6E). Pushing 2 rafts closer together forces a sharp untwisting and height variation. This increases the interfacial-twist cost, creating large gradients of twist in the interraft region, and thus increasing the strength of the repulsive interaction. In contrast to interfacial colloids, bringing rafts together cannot reduce the total area of the deformed interface, and thus does not reduce repulsions. In the previously studied chiral limit ($\phi_{ch} = 1$), the inherent chirality of the left-handed membrane background and the right-handed rafts generated repulsions because bringing rafts together reduced the preferred twist of the interraft region (29). In contrast, for an achiral membrane background ($\phi_{ch} = 0$), the chiral contribution to the interaction energy is small (Fig. 6C). In this limit, the increase in surface area and the associated excluded volume becomes the primary contribution to the repulsive interaction energy (*SI Appendix*, Fig. S3).

The continuum model also explains the attractive interactions between the L-R raft pairs. Unlike a pair of right-handed rafts, the tilt field at the inner edges of a left- and right-handed (L-R) raft pair is in the same direction, that is $\theta(-d/2,0) = \theta(d/2,0) = \theta_0$ (blue line in Fig. 6E). This removes the geometric constraint that requires rods in the interraft region to untwist completely at the midpoint, leading both to less total twist deformation and a smaller surface area (Fig. 6F). Compared with an R-R raft pair, the elastic energy of the L-R pair increases due to the counter-twisted state of one of the rafts. However, this energy increase is more than compensated by the decrease in the twist deformation that is associated with removing the constraint of rod untwisting in the interraft region (Fig. 6D). As the separation of an L-R pair increases, the rods surrounding the rafts twist back to the membrane normal and any gains in excluded volume disappear (Fig. 6G). This generates an attractive well when rafts are close enough to share their respective twist fields. LC-PolScope images reveal that the interraft region of a bound L-R pair is significantly more twisted than a twist field of an isolated raft. The model shows a similar but significantly smaller trend of increased twist between an L-R pair (Fig. 7).
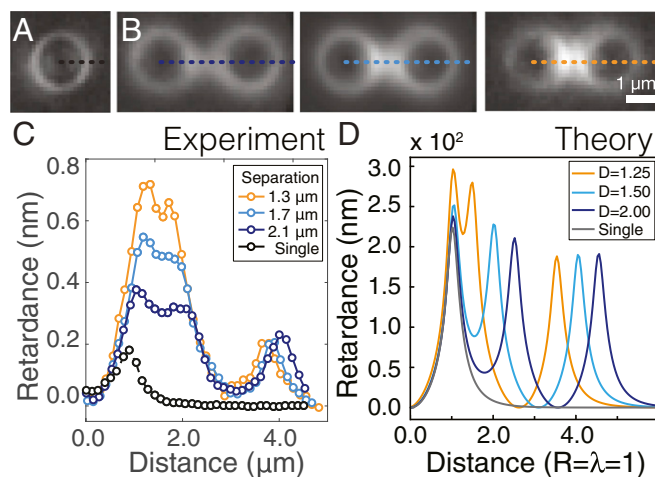

Fig. 7. Twist increases between L-R raft pairs. LC-PolScope images reveal the twist field of a single raft (A) and a L-R raft pair (B). The retardance field for separations of 2.1, 1.7, and 1.3 μm shows increasing retardance between rafts as the edge separation decreases. (C) Plot of the retardance along the midplane shown by dotted lines in A for each separation. (D) Model predictions of twist between attractive rafts also show increasing retardance as raft separation decreases, although to a lesser degree. Distances are measured in units of the raft radius, which is equal to λ, the twist penetration length for short rods.

Membrane Chirality Determines Stability of Counter-Twisted Rafts

To experimentally explore the limits of stability of the attractive L-R pairs, we systematically increased chirality of the membrane background, ϕ_{ch}. This should decrease the stability of the counter-twisted rafts, since in this case both rods within the raft and outside have to twist against their preferred handedness. We studied the stability of L-R pairs in chiral colloidal membranes ($\phi_{ch} = 0.4$). Using an optical tweezer, we switched 1 raft to a counter-twisted state and formed a L-R raft pair. Such pairs remained stably bound indicating attractive interactions, but the counter-twisted raft shrunk over time until the pair fell apart (Fig. 8 A and B and Movie S8). At this point, the 2 rafts diffused away from each other. Soon thereafter, the originally left-handed raft started to increase in size again, implying that it had switched to the energetically more favorable right-handed conformation (Fig. 8C). This indicates that the range of attractive interactions between oppositely twisted rafts is independent of the background membrane chirality, while stability of the counter-twisted rafts does depend on the chirality of the membrane background. Surprisingly, we found that counter-twisted rafts are stabilized by multiple L-R bonds, even at $\phi_{ch} = 0.4$. Specifically, we observed stable tetramers under these conditions and the higher-energy central raft remained stable indefinitely (Fig. 9 A–D). With increasing background chirality, the average size of the central raft shrank, while the outer rafts grew, to minimize the energetically unfavorable left-handed twist (Fig. 9E). Despite different raft sizes, the equilibrium separation of attractive pairs does not vary with changing ϕ_{ch}, providing further evidence that the attractive interactions do not depend on the membrane chirality (Fig. 9F).

Rafts form a variety of structures depending on short rod density and dextran concentration. The ratio of right-handed to left-handed rafts depends on raft density. The inherent preference for right-handed internal twist is only overcome by the cost of the background membrane deformation in the presence of at least one other raft. As such, the few rafts that form in membranes with a low short-rod density are unlikely to be left-handed. At high raft densities, the membrane deformation is minimized by an equal number of left- and right-handed rafts
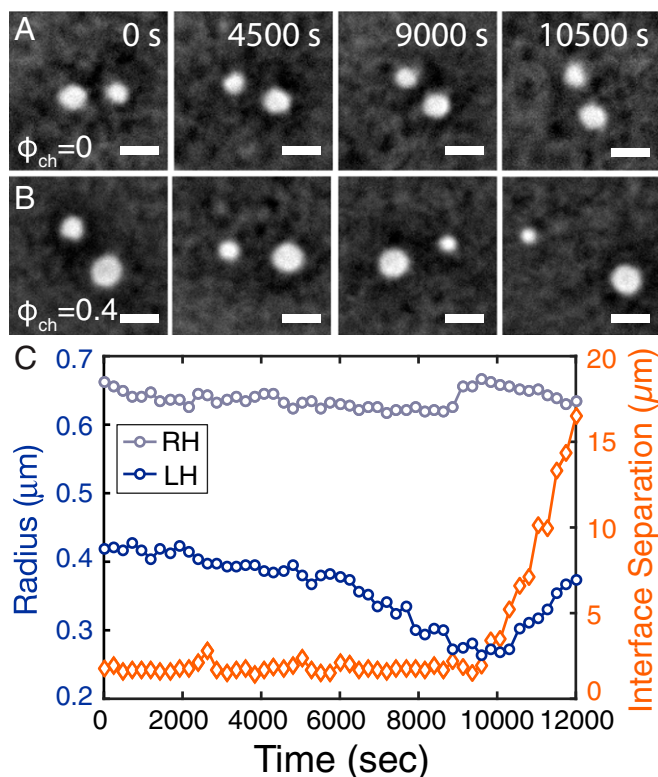
Fig. 8. A weakly chiral membrane background leads to metastable raft pairs. (*A*) In an achiral membrane background, attractive raft pairs are stable over the sample lifetime. (*B*) Increasing the left-handed chirality of the background membrane ($\phi_{ch} = 0.4$) causes the counter-twisted raft to slowly shrink over time until the pair unbinds. Once unbound, the counter-twisted raft switches handedness and recovers its original size (Movie S8). (*C*) Time evolution of the raft radii (gray and blue circles) and edge separation (orange diamonds). (Scale bars, 2 μm.)

assembled into a square lattice. Between these 2 extremes, rafts assemble into heterogeneous structures of various sizes determined by the number of left-handed rafts (Movie S1). Alternatively, rafts can assemble into chain-like structures in which links of alternating left- and right-handed rafts are joined by highly twisted necks (*SI Appendix*, Fig. S1 *A and B*). This is structurally different from the chains formed by rafts in a highly chiral background, in which each raft link has the same right-handed twist, and the rod twist is instead minimized at the necks that join the rafts (*SI Appendix*, Fig. S1D). At intermediate background chirality, the link size is anisotropic and large right-handed rafts alternate with smaller left-handed rafts (*SI Appendix*, Fig. S1C). As the dextran concentration increases, rafts become unstable in favor of bulk phase separation between long and short rods. This transition to bulk phase separation is preceded by a narrow phase space in which the left-handed rods in the achiral background mixture wet the rafts, possibly due to their chirality or comparatively low stiffness (*SI Appendix*, Fig. S2 and Movie S9).

Discussion

Our work demonstrates an intricate multistep assembly pathway of rod-like particles in the presence of depletant interactions. In a first step, isotropic bidisperse rods phase separate from the background polymer solution and form monolayer colloidal membranes. In the second step, the unique properties of the nascent 2D membrane drive lateral phase separation of short and long rods, and assembly of colloidal rafts, which are liquid-like monodisperse clusters of inclusions that contain a large but

well-defined number of short rods. Specifically, the micrometer-sized rafts we study are composed of about ~20,000 rods and can exist in 2 distinct chiral conformations. The higher-energy counter-twisted state is stabilized, at least in part, by attractive bonds formed with rafts of opposite chirality. In the final step, complex membrane-mediated interraft interactions, which are determined by the raft internal conformations, drive assembly into higher-order hierarchical structures such as highly stable tetramers and crystallites with square lattices.

Our work unifies diverse concepts from soft matter physics. By adding polymers to rod-like liquid-crystal–forming viruses, we induce assembly of colloidal monolayer membranes, which have important similarities and some distinctions with conventional lipid bilayers. Introducing an immiscible component into such membranes leads to the formation of finite-sized colloidal rafts, which have the appearance of colloid-like particles but differ in a fundamental aspect. Colloidal rafts are liquid-like deformable structures that maintain their finite size despite continuous exchange of constituent rods with the background membrane. Therefore, they are adaptable, self-healing assemblages that can sense their local environment, adjusting their structure and interactions accordingly. In this aspect, they resemble thermodynamically stable surfactant micelles. Increasing the raft concentration leads to complex clusters, whose formation is driven by emergent membrane-mediated interactions. These clusters are significantly more complex than those formed by spherical colloids under simple depletion interactions (46).

Observations of membrane-mediated assembly of colloidal rafts are intriguing from multiple perspectives. First, they demonstrate that molecular chirality provides a robust platform for rational engineering of geometrically frustrated assemblages, wherein interactions between chiral elemental units favor local packing motifs that are incompatible with uniform global order, thus generating finite-sized structures, that unlike micellar assemblies are vastly larger than subunit dimensions (e.g., rod diameters) (47, 48). Second, the interactions that we have elucidated depend only on generic properties of the membrane, such as coupling between the membrane interfacial area, the membrane thickness, and the local tilt of the constituent rods (or aligned hydrophobic chains in a lipid bilayer). Therefore, interactions similar to those
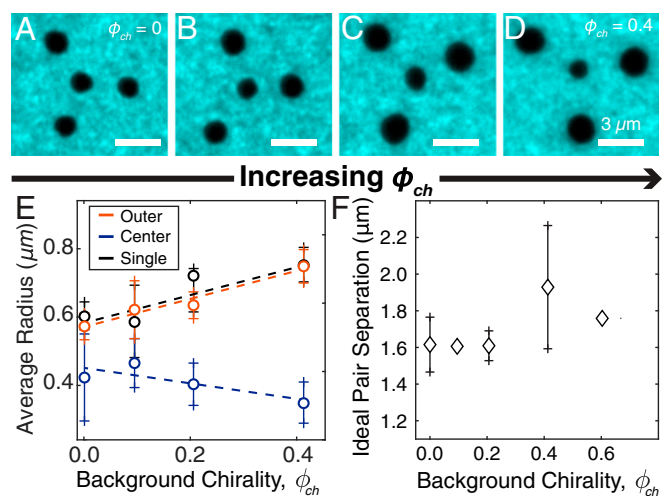
Increasing ϕ_{ch}

Fig. 9. Multiple L-R bonds stabilize counter-twisted rafts. (*A–D*) Structure of stable raft tetramers formed in colloidal membranes at different background chirality values. (*E*) With increasing background chirality (ϕ_{ch}), the size of the counter-twisted central raft shrinks and the outer rafts grow. The raft size of outer rafts in tetramer clusters is the same as those of isolated rafts. (*F*) The preferred length of a L-R bond does not depend on the background chirality.

studied here could play a role in conventional lipid bilayers, and thus be relevant for the assembly of biological membrane inclusions. Third, there is an increasing emphasis on assembling complex architectures that go beyond traditional hard-sphere crystals. The typical approach toward this goal involves developing new synthesis methods for assembly of "patchy" building blocks with complex shapes and interactions. Our work demonstrates a different route toward this goal, which uses building blocks with simple shapes. When suspended in locally structured environments, these building blocks can acquire complex interactions that drive their assembly.

Extensive work has focused on elucidating the quantitative relationship between microscopic interactions and macroscopic phase behavior, and this has guided the rational development of patchy particles. Our experiments demonstrate the richness and diversity of interactions that emerge in membrane-like environments. It thus provides impetus to use theoretical and simulation tools to fully explore the manifold of all possible interactions that can emerge in membrane-like environments. Once developed, such a theoretical framework would fully elucidate both the potential and the limitations of membrane-mediated self-assembly.

Materials and Methods

Biological Purification and Sample Prep. For our experiments, we mixed filamentous bacteriophage of various contour lengths, persistence lengths, and chirality. These mixtures were composed of *fd-wt* and M13KO7 bacteriophage which are 880 nm and 1,200 nm long, respectively. Both rods have a diameter of 6 nm, 2.8-μm persistence length, and form a cholesteric phase with a left-handed pitch. We also used the Y21M mutants of both strains, which are similar in size to the wild-type versions but have a 9.9-μm persistence length and form a right-handed cholesteric (39). We purified all strains using standard biological procedures (49). The purified virus solution generally contains end-to-end dimers and multimers that favor smectic stacks rather than monolayer membranes. We removed multimers through isotropic–nematic phase separation (27). All viruses were suspended in a 20 mM Tris·HCl buffer (pH 8.0) to which 100 mM NaCl had been added to screen electrostatic repulsion between rods.

For fluorescence imaging, we labeled the primary amines on M13KO7 with DyLight 488, and the primary amines on *fd-Y21M* with DyLight 550 (50). There are ~3,600 possible labeling sites on M13KO7 and 2,700 labeling sites on *fd-Y21M*, of which we labeled less than 2% to ensure that the fluorescent markers would not affect system behavior. In all samples, we mixed the longer M13KO7 and M13KO7-Y21M at predetermined ratio. Previous studies demonstrate that a mixture of 37% M13KO7 and 63% M13KO7-Y21M exhibits no effective chirality (40). We added *fd-Y21M* to this mixture at number ratios between 10% and 50% to form short-rod rafts within membranes.

After adding a nonadsorbing polymer (dextran molecular weight, 500 kDa; Sigma-Aldrich) to the virus mixture solution at 40 mg/mL concentration, we injected the solution into a chamber formed by a coverslip and glass slide with a Parafilm spacer. Both the coverslip and slide were cleaned with a hot soap solution (1% Hellmanex) and coated with an acrylamide brush to prevent membrane adhesion on the glass coverslip surface (36). We sealed the chamber with optical glue (Norland). The total virus mixture concentration varied between 0.5 and 1.0 mg/mL.

Microscopy. We used an inverted microscope equipped for differential interference contrast (DIC), fluorescence, LC-PolScope, and phase contrast imaging. All images were taken with a 100× oil-immersion objective (Plan Fluor, numerical aperture [N.A.] 1.3 for DIC and fluorescence; Plan Apo, N.A. 1.4 for phase) and recorded on a cooled charge-coupled device camera (Andor Clara, Neo, or iXon).

Measurements of rod tilt within membranes were taken using LC-PolScope (43). LC-PolScope uses quantitative polarization measurements to find the local birefringence of a sample. The birefringence is displayed as an image in which the pixel intensity is proportional to birefringence, which itself is proportional to the local tilt of the rods due to the liquid-crystalline nature of the membrane phase. When the membrane lies flat on the sample substrate, the rods in the membrane bulk are generally aligned along the axis of the incoming light, and the birefringence is at a minimum, leading to a low signal.

For BOT measurements, optical trap configurations were generated by time sharing a laser beam (4 W, 1,064 nm; Compass 1064; Coherent) using a pair of orthogonally oriented paratellurite acousto-optic deflectors (IntraAction). The laser beam was projected onto the back focal plane of an oil-immersion objective (1.4 N.A., 100× PlanApo) and focused onto the imaging plane. The multiple trap locations were specified by custom LABVIEW software. Because *fd-Y21M*–enriched rafts are shorter than the membrane background, the traps function as a plow that we use to push 2 rafts together or drag them apart. This enables us to watch the evolution of a raft pair after it is initialized away from its equilibrium separation. Raft separations were measured as a function of time, once the traps had been switched off, using standard video tracking methods (51). We created attractive raft pairs by pushing 2 rafts close together and then causing splay in the membrane by shifting the focus of the traps upward in *z*. When the membrane relaxed, 1 raft of the pair twisted into the metastable left-handed state. The rafts remained in the bound state for the sample lifetime. The time lapse between successive frames was 500 ms, and the exposure time was 50 ms.

The BOT measurement is based on the fact that probability of the raft separation being r_j at time $t_j = t_i + \Delta t$ can be determined by $p(r_j) = \sum_i P(r_i, r_j, \Delta t) p(r_i)$, where $P(r_i, r_j, \Delta t)$ is the transition probability for a raft pair separated by r_i at time t. We find P experimentally by binning pair trajectories by the initial and final separations for each time point. The equilibrium probability vector $\rho(r)$ is a steady-state solution to the above equation and thus can be calculated as an eigenvector of the transition probability matrix (42). Alternatively, raft pairs were tracked in equilibrium conditions over long times to calculate an effective $\rho(r)$. In both cases, we used Boltzmann statistics to calculate the effective interaction energy from the calculated equilibrium probability: $\Delta F = -k_B T \log(\rho(r))$.

1. J. N. Israelachvili, *Intermolecular and Surface Forces* (Academic Press, 2011).
2. C. Bohley, R. Stannarius, Energetics of 2D colloids in free-standing smectic-C films. *Eur. Phys. J. E Soft. Matter* **20**, 299–308 (2006).
3. I. Muševič, M. Škarabot, U. Tkalec, M. Ravnik, S. Žumer, Two-dimensional nematic colloidal crystals self-assembled by topological defects. *Science* **313**, 954–958 (2006).
4. P. Poulin, H. Stark, T. C. Lubensky, D. A. Weitz, Novel colloidal interactions in anisotropic fluids. *Science* **275**, 1770–1773 (1997).
5. B. Senyuk, Q. Liu, P. D. Nystrom, I. I. Smalyukh, Repulsion-attraction switching of nematic colloids formed by liquid crystal dispersions of polygonal prisms. *Soft Matter* **13**, 7398–7405 (2017).
6. I. B. Liu, N. Sharifi-Mood, K. J. Stebe, Capillary assembly of colloids: Interactions on planar and curved interfaces. *Annu. Rev. Condens. Matter Phys.* **9**, 283–305 (2018).
7. J. C. Loudet, A. M. Alsayed, J. Zhang, A. G. Yodh, Capillary interactions between anisotropic colloidal particles. *Phys. Rev. Lett.* **94**, 018301 (2005).
8. S. Marčelja, Chain ordering in liquid crystals. II. Structure of bilayer membranes. *Biochim. Biophys. Acta* **367**, 165–176 (1974).
9. M. Babu et al., Interaction landscape of membrane-protein complexes in *Saccharomyces cerevisiae*. *Nature* **489**, 585–589 (2012).
10. N. Dan, A. Berman, P. Pincus, S. A. Safran, Membrane-induced interactions between inclusions. *J. Phys. II* **4**, 1713–1725 (1994).
11. B. Grasberger, A. P. Minton, C. DeLisi, H. Metzger, Interaction between proteins localized in membranes. *Proc. Natl. Acad. Sci. U.S.A.* **83**, 6258–6262 (1986).
12. T. S. Ursell, W. S. Klug, R. Phillips, Morphology and interaction between lipid domains. *Proc. Natl. Acad. Sci. U.S.A.* **106**, 13301–13306 (2009).
13. P. G. Dommersnes, J.-B. Fournier, N-body study of anisotropic membrane inclusions: Membrane mediated interactions and ordered aggregation. *Eur. Phys. J. B* **12**, 9–12 (1999).
14. P. G. Dommersnes, J.-B. Fournier, The many-body problem for anisotropic membrane inclusions and the self-assembly of "saddle" defects into an "egg carton." *Biophys. J.* **83**, 2898–2905 (2002).
15. K. S. Kim, J. Neu, G. Oster, Curvature-mediated interactions between membrane proteins. *Biophys. J.* **75**, 2274–2291 (1998).
16. K. S. Kim, J. C. Neu, G. F. Oster, Many-body forces between membrane inclusions: A new pattern-formation mechanism. *Europhys. Lett.* **48**, 99–105 (1999).
17. O. S. Andersen, R. E. Koeppe, 2nd, Bilayer thickness and membrane protein function: An energetic perspective. *Annu. Rev. Biophys. Biomol. Struct.* **36**, 107–130 (2007).

18. I. Casuso, P. Sens, F. Rico, S. Scheuring, Experimental evidence for membrane-mediated protein-protein interaction. *Biophys. J.* **99**, L47–L49 (2010).

19. H. Dies, B. Cheung, J. Tang, M. C. Rheinstädter, The organization of melatonin in lipid membranes. *Biochim. Biophys. Acta* **1848**, 1032–1040 (2015).

20. C. Dietrich *et al.*, Lipid rafts reconstituted in model membranes. *Biophys. J.* **80**, 1417–1428 (2001).

21. C. A. Haselwandter, N. S. Wingreen, The role of membrane-mediated interactions in the assembly and architecture of chemoreceptor lattices. *PLoS Comput. Biol.* **10**, e1003932 (2014).

22. H. Hong, T. M. Blois, Z. Cao, J. U. Bowie, Method to measure strong protein-protein interactions in lipid bilayers using a steric trap. *Proc. Natl. Acad. Sci. U.S.A.* **107**, 19802–19807 (2010).

23. I. Levental, S. Veatch, The continuing mystery of lipid rafts. *J. Mol. Biol.* **428**, 4749–4764 (2016).

24. D. Lingwood, K. Simons, Lipid rafts as a membrane-organizing principle. *Science* **327**, 46–50 (2010).

25. S. Semrau, T. Idema, T. Schmidt, C. Storm, Membrane-mediated interactions measured using membrane domains. *Biophys. J.* **96**, 4906–4915 (2009).

26. M. B. Stone, S. A. Shelby, M. F. Núñez, K. Wisser, S. L. Veatch, Protein sorting by lipid phase-like domains supports emergent signaling function in B lymphocyte plasma membranes. *eLife* **6**, e19891 (2017).

27. E. Barry, Z. Dogic, Entropy driven self-assembly of nonamphiphilic colloidal membranes. *Proc. Natl. Acad. Sci. U.S.A.* **107**, 10348–10353 (2010).

28. Y. Yang, E. Barry, Z. Dogic, M. F. Hagan, Self-assembly of 2D membranes from mixtures of hard rods and depleting polymers. *Soft Matter* **8**, 707–714 (2012).

29. L. Kang, T. Gibaud, Z. Dogic, T. C. Lubensky, Entropic forces stabilize diverse emergent structures in colloidal membranes. *Soft Matter* **12**, 386–401 (2016).

30. M. J. Zakhary *et al.*, Imprintable membranes from incomplete chiral coalescence. *Nat. Commun.* **5**, 3063 (2014).

31. P. Sharma, A. Ward, T. Gibaud, M. F. Hagan, Z. Dogic, Hierarchical organization of chiral rafts in colloidal membranes. *Nature* **513**, 77–80 (2014).

32. L. Kang, T. C. Lubensky, Chiral twist drives raft formation and organization in membranes composed of rod-like particles. *Proc. Natl. Acad. Sci. U.S.A.* **114**, E19–E27 (2017).

33. R. Sakhardande *et al.*, Theory of microphase separation in bidisperse chiral membranes. *Phys. Rev. E* **96**, 012704 (2017).

34. Z. Dogic, S. Fraden, Development of model colloidal liquid crystals and the kinetics of the isotropic–smectic transition. *Philos. Trans. R. Soc. A* **359**, 997–1015 (2001).

35. E. Barry, Z. Dogic, R. B. Meyer, R. A. Pelcovits, R. Oldenbourg, Direct measurement of the twist penetration length in a single smectic A layer of colloidal virus particles. *J. Phys. Chem. B* **113**, 3910–3913 (2009).

36. T. Gibaud *et al.*, Reconfigurable self-assembly through chiral control of interfacial tension. *Nature* **481**, 348–351 (2012).

37. Z. Dogic, S. Fraden, Cholesteric phase in virus suspensions. *Langmuir* **16**, 7820–7824 (2000).

38. E. Grelet, S. Fraden, What is the origin of chirality in the cholesteric phase of virus suspensions? *Phys. Rev. Lett.* **90**, 198302 (2003).

39. E. Barry, D. Beller, Z. Dogic, A model liquid crystalline system based on rodlike viruses with variable chirality and persistence length. *Soft Matter* **5**, 2563–2570 (2009).

40. T. Gibaud *et al.*, Achiral symmetry breaking and positive Gaussian modulus lead to scalloped colloidal membranes. *Proc. Natl. Acad. Sci. U.S.A.* **114**, E3376–E3384 (2017).

41. S. Xie, M. F. Hagan, R. A. Pelcovits, Interaction of chiral rafts in self-assembled colloidal membranes. *Phys. Rev. E* **93**, 032706 (2016).

42. J. C. Crocker, D. G. Grier, Microscopic measurement of the pair interaction potential of charge-stabilized colloid. *Phys. Rev. Lett.* **73**, 352–355 (1994).

43. R. Oldenbourg, G. Mei, New polarized light microscope with precision universal compensator. *J. Microsc.* **180**, 140–147 (1995).

44. S. Asakura, F. Oosawa, On interaction between two bodies immersed in a solution of macromolecules. *J. Chem. Phys.* **22**, 1255–1256 (1954).

45. R. B. Meyer, *Macroscopic Phenomena in Nematic Polymers. Polymer Liquid Crystals*, A. Ciferri, W. R. Krigbaum, R. B. Meyer, Eds. (Academic Press, 1982).

46. G. Meng, N. Arkus, M. P. Brenner, V. N. Manoharan, The free-energy landscape of clusters of attractive hard spheres. *Science* **327**, 560–563 (2010).

47. G. M. Grason Perspective: Geometrically frustrated assemblies. *J. Chem. Phys.* **145**, 110901 (2016).

48. G. M. Grason, R. F. Bruinsma, Chirality and equilibrium biopolymer bundles. *Phys. Rev. Lett.* **99**, 098101 (2007).

49. T. Maniatis, J. Sambrook, E. Fritsch, *Molecular Cloning: A Laboratory Manual* (Cold Spring Harbor Laboratory Press, 1989).

50. M. P. Lettinga, E. Barry, Z. Dogic, Self-diffusion of rod-like viruses in the nematic phase. *Europhys. Lett.* **71**, 692–698 (2005).

51. J. C. Crocker, D. G. Grier, Methods of digital video microscopy for colloidal studies. *J. Colloid Interface Sci.* **179**, 298–310 (1996).

APPLIED PHYSICAL SCIENCES